ADVANCED MATERIALS TECHNOLOGIES
www.advmattechnol.de

Single-Cell Impedance Tomography Using Rolled-Up Microtubular Sensors

Sonja M. Weiz, Pallavi Jha, Kyounghun Lee, Raffael Herzer, Oliver G. Schmidt, and Mariana Medina-Sánchez**

Single-cell analysis techniques provide the opportunity to study the cellular heterogeneity that occurs between cells of the same tissue. These methods should ideally be non-destructive and label-free to allow long-term measurements that do not impede with healthy cellular functions. To that end, a miniaturized electrical impedance tomography (µEIT) system is fabricated via rolled-up nanotechnology to study the electrical properties of individual cells. The tube contains an array of 12 electrodes on its interior wall, and its diameter of ca. 30 µm is tuned to fit the size of a cell. First proof-of-concept measurements are carried out with silica and half-metal coated microparticle phantoms. Additionally, the death of a single HeLa cell is monitored with the µEIT device over time. In the future, the system can be applied to study, e.g. the efficiency of drugs or the biocompatibility of materials on a single-cell level.

1. Introduction

In recent years, there has been a rapid development of analysis techniques enabling single-cell studies.[1] Analysis methods relying on large cell cultures may seem to be more desirable at first glance, since the signal to be measured is apparently amplified due to the higher number of cells, resulting in inference of an "average" cell.[2] However, this assumption neglects the fact that not all cells within a population are identical, which is referred to as cellular heterogeneity.[3] In this manner, cell culture-scale measurements can potentially blur the small dissimilarities that can be essential for the overall behavior of the cells within an organism. Single-cell analysis devices provide high sensitivity and resolution in order to distinguish properties of individual cells, e.g. to detect abnormalities or subpopulations, which is essential for early detection and effective treatment of illnesses. Furthermore, material-cell interaction can be examined at a cellular level in in vitro biocompatibility models to reduce the risk for animals and humans in subsequent in vivo studies.[1,4,5]

Among the wide array of available analysis methods, imaging techniques are especially helpful to resolve the structural mechanism of biological processes, which helps in understanding fundamental biological research. Tomographic measurements provide spatially resolved localized information, where movements of whole cells or cell parts can be visualized. For instance, immunofluorescence techniques such as laser scanning confocal microscopy provide high spatial resolution for dynamic imaging of single cells and allow, e.g., the study of cell invasion in cancer metastasis.[6] However, labeling with fluorescent markers is required, and long-term analysis is impaired by photobleaching. Additionally, phototoxicity can occur. Furthermore, X-ray imaging and electron microscopy both allow imaging of unstained cells with high resolution, but technologically sophisticated cryo-immobilization is necessary and samples are exposed to damaging radiation.[7,8] Another biological process of interest is the cellular communication across cells that is fundamental for higher-order functions in tissues and organs and can be used to correlate

S. M. Weiz, P. Jha, R. Herzer, M. Medina-Sánchez
Micro- and NanoBiomedical Engineering Group (MNBE)
Institute for Emerging Electronic Technologies (IET)
Leibniz Institute for Solid State and Materials Research (Leibniz IFW Dresden)
Helmholtzstraße 20, 01069 Dresden, Germany
E-mail: m.medina.sanchez@ifw-dresden.de

K. Lee
Department of Computational Science & Engineering
Yonsei University
Seoul 120–749, South Korea

O. G. Schmidt
Leibniz IFW Dresden
Helmholtzstraße 20, 01069 Dresden, Germany
E-mail: oliver.schmidt@main.tu-chemnitz.de

O. G. Schmidt
Research Center for Materials
Architectures and Integration of Nanomembranes (MAIN)
Chemnitz University of Technology
Rosenbergstraße 6, 09126 Chemnitz, Germany

M. Medina-Sánchez
Chair of Micro- and NanoSystems
Center for Molecular Bioengineering (B CUBE), and Dresden University of Technology (TU Dresden)
01062 Dresden, Germany

The ORCID identification number(s) for the author(s) of this article can be found under https://doi.org/10.1002/admt.202300724

DOI: 10.1002/admt.202300724

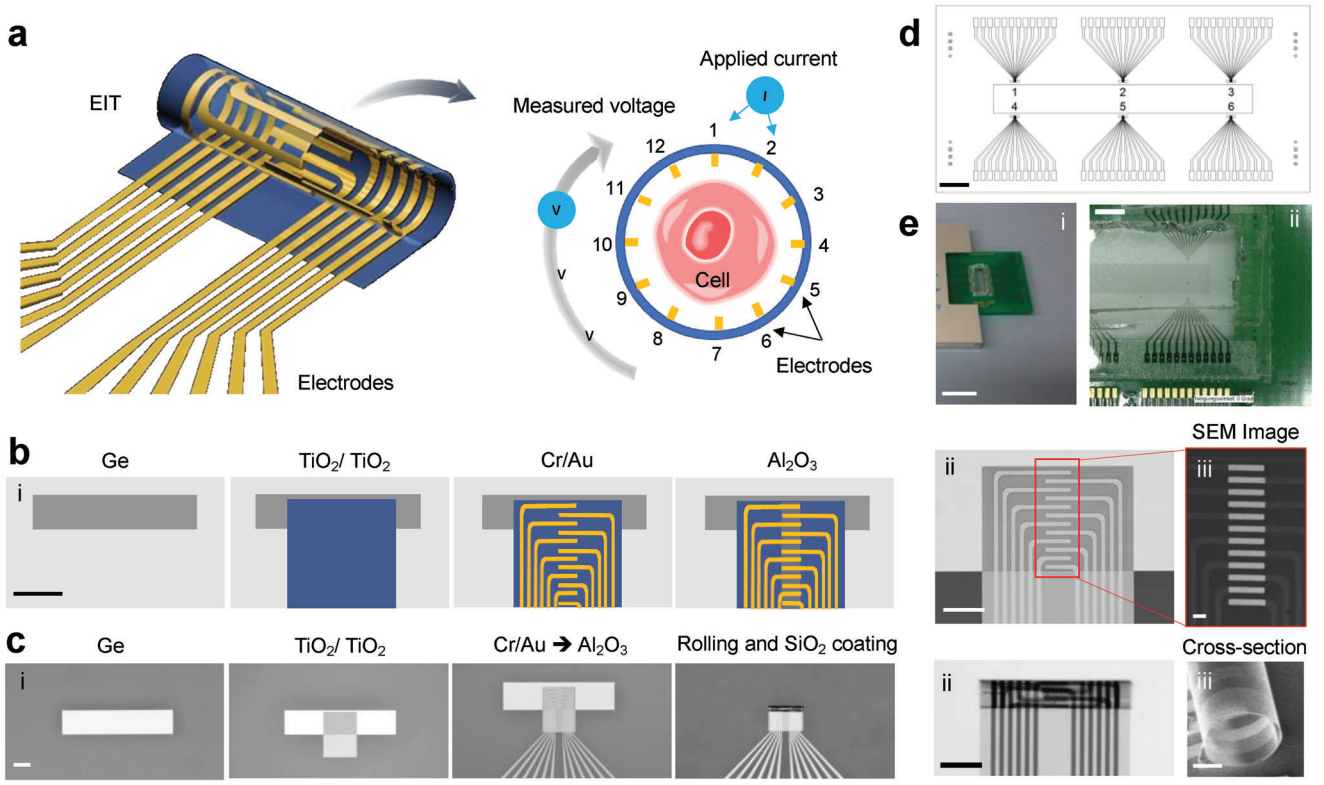

Figure 1. Microscale rolled-up EIT device. a) Conceptual image of the microscale tomography device with an array of 12 electrodes encompassed all around the inner part of the tube, and the corresponding cross section indicating the location of a model sample (e.g., a cell). Then, a current is applied in a pair of electrodes and the corresponding voltage drops among all possible combinations of the remaining electrodes are recorded to form a reconstructed cross-section conductivity map. b,c) Fabrication steps of the rolled-up microscale EIT (i), scale bar: 100 µm. The images in the right side show the planar and rolled-up structures (ii), scale bar: 50 µm. SEM image in back scattering mode indicates the proper passivation of the contact pads (dark) and the exposed detection areas (bright) before rolling, and the tube cross-section is also shown with an SEM image indicating a diameter of ca. 30 µm (ii), Scale bar: 10 µm. d) Layout of a chip containing six microtomography devices. Scale bar: 2 mm, and e) the resulting chip wire bonded to a PCB which is then plugged into a chip connector for the consequent impedance measurements. Scale bars: i) 2 cm, ii) 2 mm.

these electrical signals with diseases such as arrhythmias. This communication can be studied at the cellular level by means of electrophysiological methods, e.g., detection of individual ionic currents across the cell membrane by monitoring the field potentials from a 3D spheroid encapsulated in tubular microelectrode array.[9]

Electrical impedance tomography (EIT) presents an attractive alternative approach, where multi-electrode measurements are carried out to image the conductivity distribution of an object.[10] The largest drawback of impedance measurements compared to the previously mentioned analysis methods is the lower image resolution. However, depending on the application, this disadvantage can be outweighed by the benefits: the technique is label-free, non-destructive, is susceptible to miniaturization, provides real-time information due to rapid data collection, is comparatively cheap and allows long-term monitoring since there are no known hazards.[11] Notably, electrical impedance tomography provides spatially resolved conductivity information, allowing to correlate the visualized movement of whole cells or cell parts with underlying physiological processes. The technique has found great use in a medical setup such as pulmonary or gastric imaging but majorly for monitoring neural activity. Several studies have investigated the application of EIT in studying brain activity, particularly during epileptiform events,[12–14] and evoked[15,16] physiological responses in rat models, demonstrating the versatility of EIT to capture rapid as well as diverse neural responses. Some studies have also examined the frequency-dependent changes in impedance in similar conditions.[16] Inspired by the diversity of EIT applications, novel endeavors have been made to develop miniaturized systems to visualize neural activity, image material transport in microfluidic channels or monitor electroporation in real-time.[17–19] However, while single large slime mold cells (*ca.* 2 mm diameter) were imaged,[20] none of the previously described devices was small enough to analyze a single animal or human cell, whose size typically lies in the range of 10–20 µm. To that end, we have prepared a novel EIT sensor in the sub-100 µm size range based on the self-assembled roll-up of strained nanometer thin films.[21,22] Using standard microfabrication techniques, such as photolithography and thin film deposition, we were thus able to pattern an EIT electrode array into a small 3D structure (**Figure 1**a). To perform imaging, an alternative current was applied to a pair of electrodes (e.g., 1 and 2 in Figure 1a) and voltages across sequential electrode-pair combinations were recorded to further reconstruct a map of conductivity distribution of the measured object/cell. This approach provides many advantages and possibilities. First, 3D devices on the

size scale of single cells can be fabricated in a simple, straightforward and flexible manner, where parameters like tube diameter as well as number and arrangement of electrodes can be easily varied. Similar 3D devices with tubular electrodes have been used as impedance spectroscopy sensors for immune cell analysis,[23] and for investigating viability of cancer cells in presence of an anticancer drug[24] or in conjunction with tubular waveguides as high-throughput cell counters.[25] The choice of transparent tube materials allows simultaneous optical observation. Furthermore, it has previously been shown that the tubular geometric configuration both increases the sensitivity of integrated electrodes[26,27] and mimics the cells' in vivo constraints, thus enabling measurements under physiological conditions.[28] As a proof of concept, in this work, we employed the proposed system to image silica particles, Janus particles, and cancer cells. We demonstrate the versatility of the technique to measure conductivity changes of living biological samples over time as shown for cell necrosis sensing. In future, the system can be employed to analyze the effect of drugs or surrounding environment on the cell behavior in live and real-time imaging (without employing toxic labels or needing sample fixation).

2. Results and Discussion

2.1. μEIT Device Fabrication

The μEIT devices were fabricated using rolled-up nanotechnology as described elsewhere.[26,27] In brief, a sequence of photolithography and electron-beam deposition steps were carried out to pattern a germanium (Ge) sacrificial layer, a strained bilayer of titania (TiO_2), a chrome/gold (Cr/Au) electrode array, an aluminum oxide (Al_2O_3) coating to define the detection windows, and a silica (SiO_2) stabilizing layer (Figure 1b,c). With the insulating layer, the size of the individual microelectrodes was defined to be 5 µm by 30 µm (SEM Image, in Figure 1b(ii),(iii)). The design of the electrode array, seen **in** Figure 1b(ii), was intentionally chosen to achieve an active area similar to the HeLa cell diameter of 25 µm (Figure S1a,b, Supporting Information). The design also resulted in a higher imaging resolution as the cross-section of all 12 electrodes coincided in a single imaging plane at the center as compared to another alternative electrode array that only had 4 electrodes per imaging plane as shown in Figure S2a,b (Supporting Information). After the fabrication of the microelectrodes, when the substrate was immersed in a diluted solution of hydrogen peroxide, the Ge layer was etched selectively, and the released TiO_2 layer rolled up to form a microtube with a diameter of *ca.* 30 µm (Figure 1c(ii),(iii). The final diameter of the rolled tube is influenced by a number of factors depending on the material composition of the tubes. Previous studies on various self-rolling tubes, including metal, organic, inorganic/organic hybrid tubes have demonstrated that the strain can be introduced and controlled in the bilayer by regulating the thickness of the layers,[29,30,31] deposition parameters,[32] external stimuli,[33] or pH.[34] For the microtubes in this work, the control on the diameter was achieved by modulating the layer thickness and metal and oxide deposition rates. Thus, by optimizing these parameters, microtubes with a diameter of c*a.* 30 µm were fabricated. The average diameter was calculated from multiple successfully rolled tubes shown in Figure S3 (Supporting Information). After the rolling process, critical point drying was carried out to avoid collapsing of the microstructure, which was then covered with an additional layer of SiO_2 to increase its mechanical stability. The resulting structure possessed an integrated array of 12 electrodes arranged periodically around the tube circumference, thus surrounding any object inserted into the µEIT device. The fabrication of such EIT devices can be scaled-up (also see Figure S4, Supporting Information), as shown as proof of concept with the fabrication of an array of six microscale EIT devices on a single chip, which was then wire bonded to a PCB designed for a plug-in connection to the measuring device (Figures 1d,e). Details of the device fabrication are found in the Experimental Section.

2.2. μEIT Electrode Characterization

The fabricated electrodes were characterized by cyclic voltammetry, showing a clear linear response when varying the concentration of potassium hexacyanoferrate (II)/hexacyanoferrate (III) (Fe^{2+}/Fe^{3+}) solution mixed in 0.1M KCl, in a range between 8 to 1000 µM, obtaining a detection limit of ca. 17 µM, 4.3 times lower than their planar counterparts (**Figure 2**a(i); Figure S5a, Supporting Information). This limit of detection was calculated following the 3σ/slope criterion of the International Union of Pure and Applied Chemistry (IUPAC).[35] Another observation when comparing the same concentration range is that signal-to-noise ratio is higher in tubular than in planar electrodes, as the tubular configuration is very efficient in canceling the external noise, as it was previously observed for interdigitated electrodes.[27] The same concentration range was measured by electrical impedance spectroscopy (EIS), showing also a linear response and high reproducibility, reaching limits of detection of ca. 8 µM compared to 117 µM for the planar geometry (Figure 2a(ii); Figure S5b, Supporting Information). In order to confirm the consistency of the overall fabrication process, the measurement stability and repeatability of both tubular and planar electrodes are also shown in Figure S6a–d (Supporting Information).

The rolled-up EIT devices were tested using Janus particles with one conductive and one dielectric side. These were fabricated by partially covering silicon dioxide microspheres (diameter *ca.* 20 µm) with a 5 nm chromium and 50 nm gold layer. After introduction into the tubular electrode with a micromanipulator, cyclic voltammetry and impedance measurements were carried out in aqueous solution of Fe^{2+}/Fe^{3+} (1 mM) in 0.1 M KCl. The particle was then removed, and the measurement was repeated. Electrode 5 was used as reference and counter electrode, while electrodes 1–4 and 7–12 were used as working electrodes (electrode 6 was disregarded because of damaged contacts). As it is observed in Figure 2b(i),(ii), cyclic voltammogram (CV), Bode and Phase plots show differences depending on the presence of a particle inside the tube. For all electrodes, the CVs exhibited lower oxidation and reduction peak currents with the inserted Janus particle. This is attributed to the particle partially blocking the electrode surface, thus hindering the diffusion of the redox species (Figure 2b(i)). In Figure 2b(ii) in the Bode plot one can observe that major differences were obtained within the frequency range between 100 Hz and 100 kHz. For further analysis, the

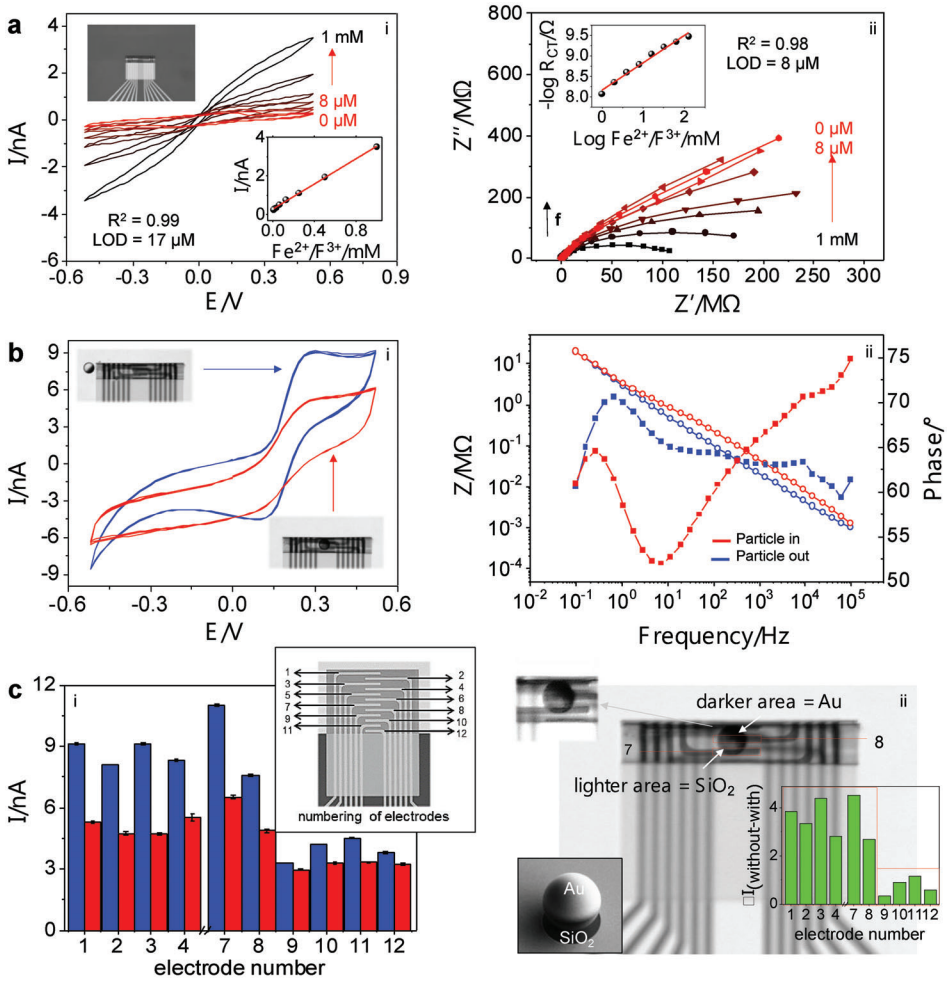

Figure 2. Microscale rolled-up EIT electrical characterization. a) Cyclic voltammogram (i) and Nyquist plot (ii) for varying Fe^{2+}/Fe^{3+} concentration. b) Cyclic voltammetry (i) and Bode/Phase plots (ii) obtained with (red lines) and without (blue lines) Janus particle inside the device. c) Absolute values (i), and difference (ii) in oxidation peak current observed for individual electrodes in measurements with and without introduced particle, respectively. Electrodes 1–8 were in proximity to dielectric part, electrodes 9–12 to conductive part of Janus structure. Janus particle diameter: 20 μm.

oxidation peak current at 0.35 V was considered. When comparing the difference of the peak currents ΔI with and without introduced particle for the individual electrodes, two distinct groups with similar Δ*I* values could be made out (see Figure 2c(i),(ii)). These groups correspond to electrodes that were close to the conductive part of the Janus particle (electrodes 9–12) and electrodes close to the dielectric area of the particle (electrodes 1–8). In the first case, a regeneration of the reduced species occurred at the conductive surface of the particle. This partly compensated the hindered diffusion due to the presence of the particle, leading to a smaller Δ*I*. In the second case, where the electrodes were close to the silicon dioxide part of the particle, this regeneration did not occur. The electrode blockage came to full effect, resulting in a larger Δ*I*. The impedance measurements with and without the Janus particle at two different frequencies, 10 Hz and 100 kHz, shown in Figure S6e,f (Supporting Information) also confirm the electrode blockage effect due to the presence of the Janus particle as the impedance values increased for all measured electrodes in comparison to the empty tubular electrodes.

2.3. EIT Tomography and Detection Modes

EIT tomography is a non-invasive technique that allows the imaging of conductivity, permittivity and impedance maps of an object/sample of interest, properties that depend on the sample free ion content. The proposed device in particular permits the monitoring of small objects or single cells (in the size range of *ca.* 20–30 μm diameter). It involves the application of small alternative currents at various frequencies. The resulting equi-potentials (voltages) are then recorded from the remaining pairs of electrodes (all electrodes except the pair where a current is applied). This process is iterated until all electrode pairs are used. Data collection varies according to the intended application. There are three reported modes: first, the absolute or static EIT (a-EIT) is used to measure the absolute conductivity distribution of the analyzed sample.[36] However, due to the fact that electric currents travel along the path of least resistivity, and biological samples are heterogenous and inter- and intra-individual differences exist among electrode conductivity, partial losses of the electrical current might be produced leading to noise and

image artifacts.[11,37,38] Differential EIT measurement modes have been developed to overcome the above-mentioned limitations, by recording data of the same sample between two or more different states.[11] For example, time-differential EIT (td-EIT) measures conductivity as a function of time, monitoring physiological processes (e.g., breathing, digestion). Another differential EIT mode is based on frequency-difference EIT (fd-EIT), which is the imaging of the conductivity as a function of frequency, considering that tissue/cell conductivity is frequency dependent.[38] This mode is also very often used to remove artifacts due to geometry or electrode conductivity variations. In this work we mainly employed fd-EIT for phantom sample characterization and td-EIT for cancer cell death monitoring over time.

The image reconstruction in EIT involves reconstructing the conductivity distribution based on the geometry of the sample, injected current values and patterns, and the measured surface voltages.[36] The correlation between change in voltage measured on the surface, based on the current injection pattern and the conductivity distribution or change is given by a linear approximation:

$$\Delta\vec{v}_m = J\Delta\vec{\sigma} \tag{1}$$

where $\Delta\vec{v}_m$ is the voltage change measured on surface, J is the sensitivity matrix and $\Delta\vec{\sigma}$ is the change in conductivity in the imaging domain. In order to make this linear approximation, the imaging domain is assumed to be made of discrete finite elements. This discretization of the imaging domain results in the sensitivity matrix J that is given by the following matrix:

$$J = \begin{bmatrix} \frac{\Delta\vec{v}_1}{\Delta\vec{\sigma}_1} & \cdots & \frac{\Delta\vec{v}_N}{\Delta\vec{\sigma}_1} \\ \vdots & & \vdots \\ \frac{\Delta\vec{v}_1}{\Delta\vec{\sigma}_Z} & \cdots & \frac{\Delta\vec{v}_N}{\Delta\vec{\sigma}_Z} \end{bmatrix} \tag{2}$$

where Z is the number of finite elements and N is the number of transfer impedance measurements done for the imaging domain. Based on equation X, in order to recreate the conductivity distribution from the surface voltage measurements, the sensitivity matrix needs to be inverted. However, this matrix is degenerate and hence, not invertible. Conventionally, the alternative is, therefore, to create a regularized inverse of the sensitivity matrix with a regularization operator and regularization parameter, both represented by R_{FE} and λ respectively. Then, the reconstructed conductivity change ($\Delta\vec{\sigma}_{recon}$) in the imaging domain is given by the following equation:

$$\Delta\vec{\sigma}_{recon} = \left(J^T J + \lambda R_{FE}^T R_{FE}\right)^{-1} J^T \Delta\vec{v}_m \tag{3}$$

where J^T and R_{FE}^T are the transpose matrices for the sensitivity matrix and the regularization parameter. However, for this work, the image reconstruction based on the conductivity distribution was done using Electrical Impedance Tomography and Diffuse Optical Tomography Reconstruction Software (EIDORS) using a fidelity-based regularization algorithm that bypasses the need to inverse the sensitivity matrix. The algorithm results in increased robustness and fidelity in image reconstruction as it is independent of the choice of the regularization parameter. Instead, the algorithm incorporates the shape of the sensitivity matrix in the regularization process. The algorithm is particularly useful for medical applications as it does not require any adjustments in the regularization parameter for different samples. A simplistic flow for one of the strategies used for the raw EIT data acquisition, followed by the image reconstruction and the post-processing steps is shown in **Figure 3**. The measurement is carried out by applying a small alternating current to a pair of adjacent electrodes and the resulting surface voltages are measured at the remaining electrodes. This is repeated for different adjacent pair combinations to acquire information about the heterogeneity in conductivities across the sample. Once the raw data is acquired, the image reconstruction is carried out using the EIDORS software (more details in the Experimental Section). The boundary artifacts can be removed using a boundary filter with variable strengths and it reduces current injection artifacts. However, using a very high strength boundary filter could result in loss of key information from the sample's core.

2.4. Phantom Measurements with the μEIT Device

Measurements were carried out with an EIT system with a customized chip adapter (Sciospec Scientific Instruments). A 1X phosphate buffered saline (PBS) solution was first used as an electrolyte, and SiO_2 microparticles with different diameters were introduced into the middle of the rolled-up tube with the help of a micromanipulator (see Figure S7, Supporting Information). Current injection occurred between adjacent electrodes (11 µA, 1–100 kHz). The frequency range chosen for EIT measurements depends on the information that needs to be extracted from the analyte. When an electric field is applied, the energy of this applied electric field can either be dissipated or stored. In case of dielectric material such as cell membranes, the impedance is directly related to its permittivity.[39] The relative permittivity, in general, is frequency dependent and for cells and tissues in solution, the relative permittivity varies largely in four frequency ranges.[39–41] Briefly, α-dispersion that happens below 10 kHz, gives information about ion diffusion across the cell membrane. The β-dispersion below 10 MHz arises mainly due to membrane polarizations, and specifically around 10 kHz, the conductivity changes are associated with the membrane integrity.[39–41] The δ and γ dispersions at much higher frequencies occur mainly due to the polarization of water molecules and therefore do not provide much insight into cellular changes.[40] Also, at such high frequencies, alienating medium contributions from cell/tissue contributions is challenging. Since the current work focused on cell membrane disintegration upon cell swelling, the frequency range from 1–100 kHz was chosen to monitor the cell-membrane integrity. The existing literature on cell studies using EIT also focuses on this frequency regime that is different from the frequency ranges chosen for monitoring neural activity where the principle relies on low frequency currents below 100 Hz that are confined into the extracellular space.[42] For first fast inspections, we employed only 8 of the 12 available electrodes. EIT image reconstruction was carried out using a fidelity-embedded regularization (FER) method as reported elsewhere.[43]

Figure 4a shows optical microscopy images of SiO_2 microparticles with diameters of 21 and 12 µm, respectively, inside

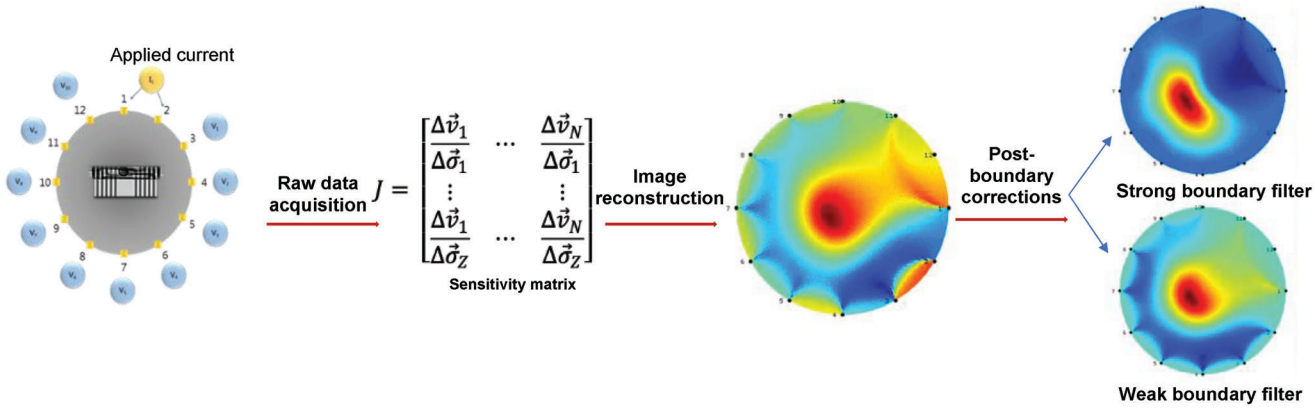

Figure 3. The raw data acquisition involves injecting current to two adjacent electrodes as shown in the first image. Measured data is stored in the form of a matrix, which contains the boundary conditions at each excitation site. Subsequently, the image reconstruction using EIDORS software generates a cross-sectional image. Post-boundary corrections are done to eliminate boundary artefacts. The effects of varying filter strengths are shown in the final image, underscoring the impact of the filter strength on the quality and fidelity of the final image.

the same tubular μEIT devices, as well as the resulting EIT image. The overlaid black circle corresponds to the actual particle size determined from the optical images. These measurements show that not only the presence of an object inside the rolled-up μEIT device can be detected, but also that particles with different sizes can be distinguished qualitatively, showing the suitability of the system for small objects/sample characterization. In the next step, the medium and injection pattern needs to be defined for single-cell EIT measurements. Cell medium has a complex chemical composition as it contains, e.g., nutrients and antibiotics. To avoid interference during electrochemical measurements due to the high number of different compounds, PBS electrolyte solution was used instead during EIT analysis. While undiluted 1X PBS solution is isotonic to the human body,

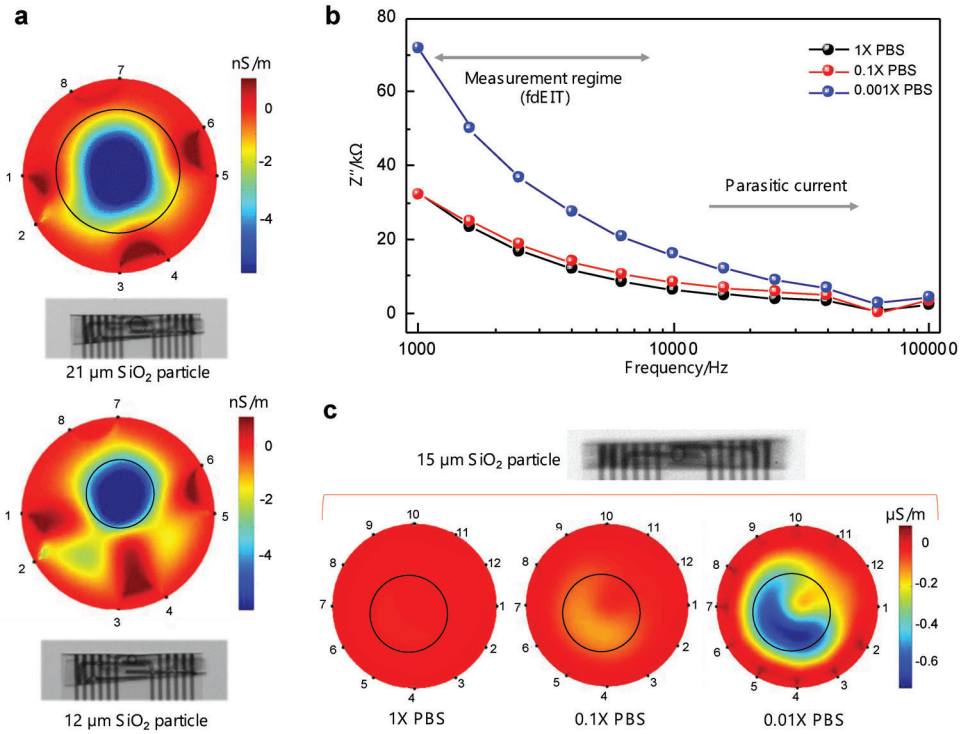

Figure 4. EIT measurements optimization. a) Optical microscopy and frequency-difference EIT images (at 1 kHz, reference 10 kHz) of SiO_2 microparticles with different diameters. b) Bode plot in the frequency range between 1–100 kHz for different conductive strength electrolytes, indicating that at higher frequencies no matter the electrolyte conductivity, the response reaches the same values. This information provides a suitable frequency range to perform the differential EIT image acquisition (c). Depending on the analyzed object, a proper selection of fluid conductivity should be taken into consideration.

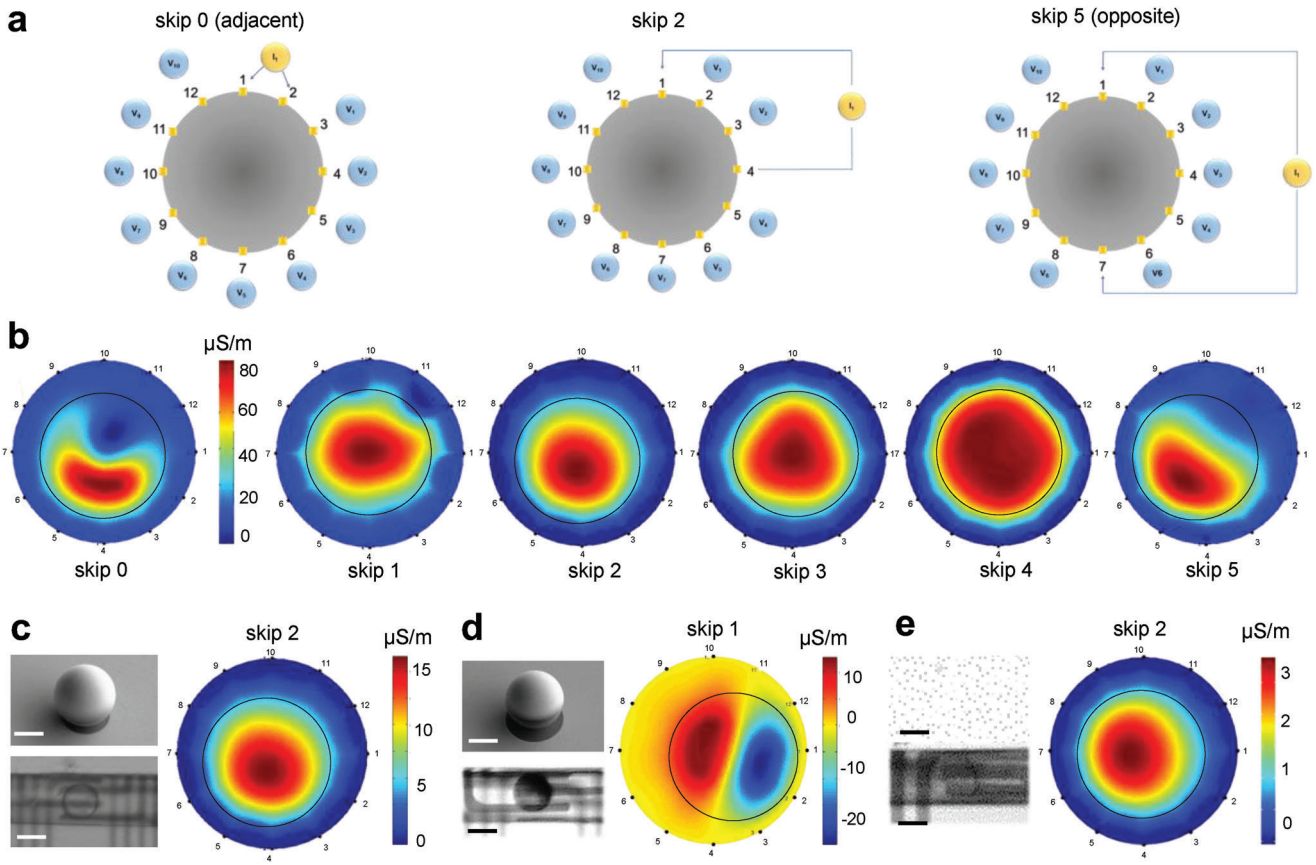

Figure 5. Injection pattern evaluation on the resulting EIT reconstructed image. a) Schematic of three exemplary injection patterns, with the adjacent one (skip 0) more sensitive to boundaries or objects close to the electrode surface, skip 2, an injection pattern with a good compromise between sensitivity and some surface details sensing capabilities, and skip 5, also called opposite injection pattern, which has more penetration depth but which is also compromised by the applied frequency and electrode design. b) An exemplary sequence of SiO_2 particle tomography images, changing the injection pattern. c) Results for SiO_2 particles employing skip 2, d) Results of a Janus particle with better results using skip 1, and e) Cell image employing skip-2. Scale bars in c, d, e: upper image: 5 μm, lower image: 20 μm.

lower salt concentrations are beneficial in electrochemical analysis, which has been shown to enhance electron transfer. To determine a suitable concentration to allow for high-sensitivity measurements, Bode plots were measured in 1X, 0.1X and 0.01X PBS concentrations, as shown along with the corresponding EIT images in Figure 4b,c.

While 1X and 0.1X PBS show a similar frequency response, a steeper slope is observed for the 0.01X dilution. Since this corresponds to a larger contrast in frequency-difference imaging, the 0.01X PBS concentration was chosen as a medium for the following EIT analysis. This concentration was also chosen for this work for inducing cell necrosis, which is discussed later in the manuscript. The use of 0.01X PBS solution resulted in cell shrinking and membrane rupture over time that could be distinguished from the live cell due to the conductivity variations in the EIT image (shown in Figure 6a,b). The EIT image in Figure 4c also underscores the higher sensitivity of the 0.01X PBS solution in this scale range, in contrast to 1X PBS solution, where conductivity variations at the core and the surface of the SiO_2 particle were less pronounced. However, it is important to emphasize that if the measurement scale is changed, as shown in Figure S8 (Supporting Information), the EIT signal is still sensitive enough to detect the variations in conductivity even in 1X PBS. These results show that 1X PBS solution could be used for future experiments.

Initial tests of the microtubular EIT device were carried out with a variety of different injection patterns. Previously, it was shown that adjacent injection leads to higher sensitivity at the boundary of the sampling volume, while skip-patterns are more sensitive to internal changes.[38] Silicon dioxide particles, Janus particles and single HeLa cells were imaged with the microtubular EIT device in 0.01X PBS with adjacent and skip-n current injection patterns (n = 1-5, with skip-5 corresponding to injection using opposite electrode pairs) (**Figure 5**a,b). As shown in Figure 5b, for adjacent injection (skip 0) the reconstructed image exhibits an artefact, since the spherical particle appears crescent-shaped. This effect is attributed to the tubular structure, where the winding layer may cover the lowermost electrode during the rolling process. The skip-1 to skip-4 injections more accurately represent the shape of the objects, with skip-2 showing the most accurate size correspondence in the case of the SiO_2 particle and HeLa cell, and with skip-1 for the Janus particle (black overlay, actual particle and cell size determined by optical microscopy). Since the skip-methods are more sensitive to internal changes

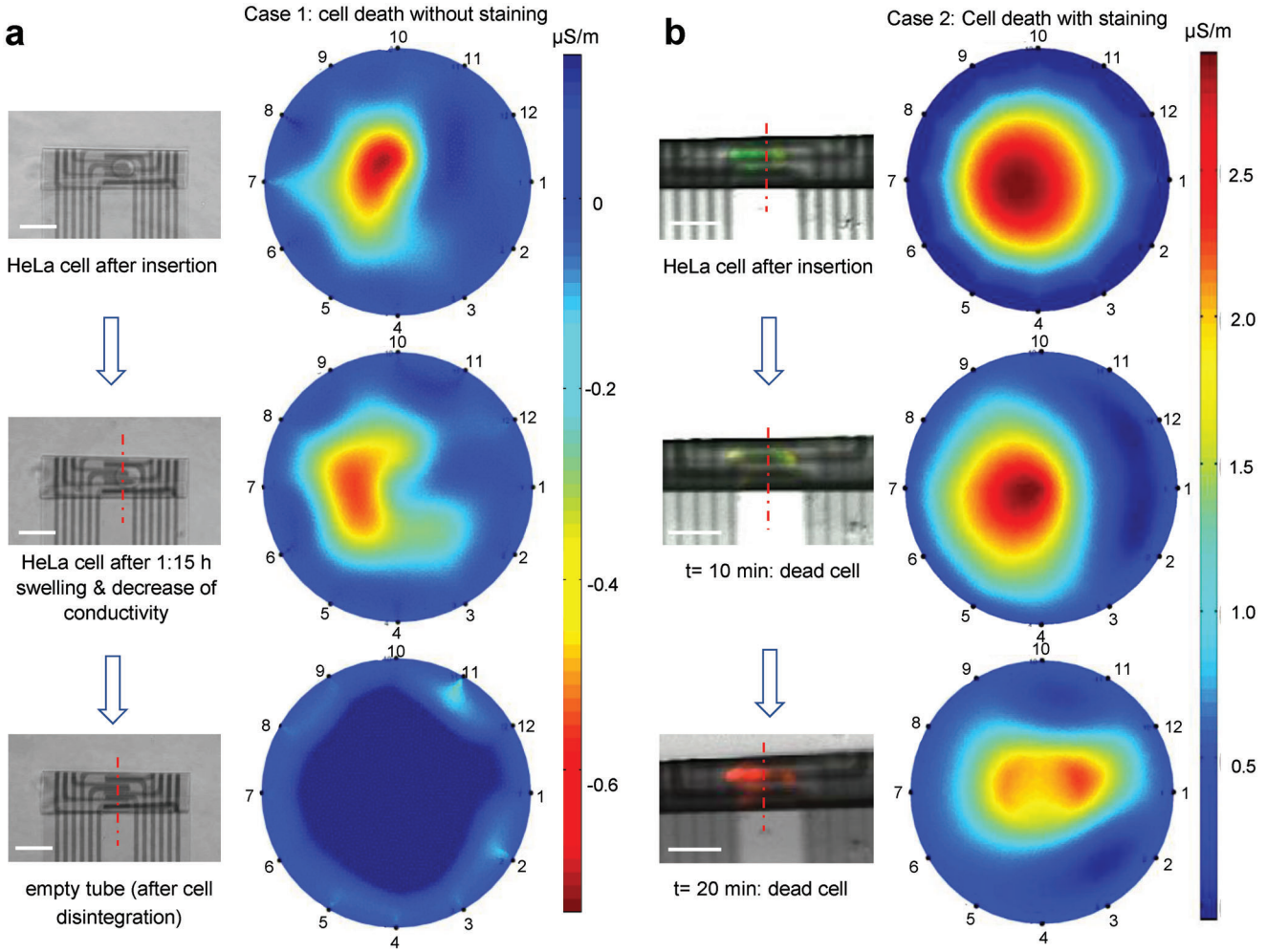

Figure 6. Optical microscopy and corresponding frequency-difference EIT images at 1 MHz, reference 5 kHz. a) From left to right: a healthy HeLa cell just after insertion, a swollen cell during necrotic death and the empty µEIT tube after cell disintegration (after ca. 2 h inside the microtube). Scale bar: 20 µm. The cell was highlighted in red in the optical microscopy images for increased visibility. b) Imaging of a stained cell to verify time of cell death via fluorescence spectroscopy. Scale bar: 25 µm. The measurements were carried out in 0.01X PBS solution.

in the measurement volume, it is possible to compensate for the artefact caused by the covered electrode in this manner. As proof of concept, silicon dioxide particle phantoms were imaged in PBS medium. Figure 5c–e shows the comparison between SiO_2 particle, a Janus particle and a HeLa cell, with their corresponding reconstructed conductivity map. Results using skip 1 to 5 for each of the analyzed samples: silica particle, Janus particle, and HeLa cell, are shown in the Figures S9 and S10, Supporting Information.

2.5. Detection of Cell Death Using the *µ*EIT Device

To show the suitability of the device for the analysis of single cells, a HeLa cancer cell was introduced into the micro-tube using a micromanipulator. The insertion procedure was performed by employing a glass capillary, securely attached to the micromanipulator. This pipette was then utilized to gently maneuver a single cell into the microtube, as shown in image sequence of Figure S7 (Supporting Information). This insertion procedure ensured the cell's integrity and viability, as the cell is not introduced into the pipette tip. The cell's viability after insertion is also confirmed by the green fluorescence from the stained cell in **Figure 6**b (top right). A close-up view of the stained cell after insertion is also included in Figure S11 (Supporting Information). EIT measurements were carried out with adjacent current injection (1 µA, 100 Hz-1 MHz, see Figure 6a; Figure S12, Supporting Information). The sample was immersed in a 0.01 X PBS electrolyte solution without additional nutrients in the medium, which over the course of several hours leads to necrotic cell death. During necrosis, the cellular membrane becomes permeable to the outside medium, leading to irreversible swelling and finally to total loss of membrane integrity.[44] In the EIT image of the healthy cell, taken immediately after insertion, the cytoplasm is visible as a region with high conductivity; where warmer colors represent higher conductivity regions and vice versa. During the swelling process, the cell takes up the low-conductivity PBS medium, which is expressed as a conductivity reduction,

quantified by a 6.7% increase in the mean gray value that represents an increase in cooler colored areas, i.e., low-conductivity regions in the EIT measurements. Once the cell is disintegrated after necrosis, the tube appears empty in the optical microscope, and no region of increased conductivity is visible anymore in the EIT image.

We then analyzed the applicability of our microtubular EIT sensor to image the death of a single cell. An established procedure to visualize and quantify this process is fluorescence staining, which was used as a control. However, staining for live/dead viability tests is typically an endpoint analysis (Figure 6b). While continuous measurements are possible, there is a severe drawback of fast photobleaching of the staining components, resulting in low fluorescence intensities over time. EIT measurements are an attractive alternative due to their label-free nature. After cell culture, suspended HeLa cells were introduced into 0.01 X PBS solution without the addition of supplemental nutrients. These conditions gradually resulted in cell death. The fast photobleaching of the stain, occurring within minutes, represented a challenge, since the fluorescence intensity decreased even during the short time required for cell approach and manipulation into the tube.

In the optical images, swelling and disintegration of the cell was observed due to necrosis. During necrotic swelling, the cell membrane becomes permeable to the outside and takes up the surrounding low-conductivity PBS solution, resulting in the observed conductivity decrease, i.e., reduction in warmer colored regions in the EIT images after 10 min and almost no regions of high conductivity were seen after 20 min. It is confirmed with a 15% and 18% increase in mean gray values after 10 and 20 min of inserting the stained cell respectively. This decrease during cell death was observed for all tested injection patterns, with geometry artefacts occurring for adjacent and opposite injections (Figure 6b; Figures S13–S16, Supporting Information).

3. Conclusion

In conclusion, the presented device, consisting of a self-rolled microtube with an integrated array of electrodes, constitutes the smallest EIT sensor developed to date. It enables the label-free and non-invasive visualization of objects in the 10–30 µm range, i.e., the size scale required for analysis of individual biological cells. It was possible to image the death of single HeLa cells, thus opening the door to track other physiological processes, such as metabolic changes during therapeutic treatments.

Rolled-up nanotechnology gives access to powerful sensing devices on the micrometer scale. By including an array of microelectrodes into the rolled-up structure, a miniaturized EIT device was fabricated, with which the size difference of silica microparticles, as well as necrotic cell death of a single HeLa cell, could be visualized. Unlike planar EIT devices, the structure presented here approaches cellular measurements under in vivo-like conditions, due to the geometric constraints introduced by the microtube. The work presented herein therefore represents a step toward body-on-a-chip devices. Studies focused on single-cell analysis methods play a critical role in advancing various fields of research and applications encompassing life sciences, biomedicine, and beyond. Therefore, further improvements in the device will also focus on expanding the applications of this microtubular EIT device. The potential integration of this device with microfluidics will significantly enhance throughput, enabling the concurrent study of numerous individual cells. It will help us to investigate cellular heterogeneity and response variations within larger populations.

The principle of EIT imaging in conjugation with our microtubular device can also be extended to larger specimens, such as tissues or developing embryos, where complex topography and conductivity distributions necessitate a cellular-lever perspective. In the realm of drug development, single-cell analysis allows the assessment of cellular responses to potential drugs,[41] optimizing drug selection and exploration of drug-resistance mechanisms. The device could also be used for microparticle analysis, including functionalized microparticles or Janus microrobots. This field could benefit greatly from single-cell analysis as it allows the examination of individual particles and their interaction with biological entities. This could have far-reaching implications in field like nanomedicine and targeted drug delivery. Additionally, implementing strategies for cell or particle rotation, spatially-resolved impedance measurements hold the potential to improve their characterization by enabling 3D property mapping. In essence, this microtubular EIT device open numerous avenues for research not only in cellular behavior but also support the advancement in biomedicine, healthcare, and biotechnology.

4. Experimental Section

Sensor Fabrication: Microtubular EIT devices were prepared similarly as described previously.[26,27] In short, alternating steps of photolithography and material deposition via electron-beam or atomic layer deposition were carried out to pattern, successively, a sacrificial germanium layer (20 nm), a strained titanium dioxide bilayer (60 nm), an electrode array (5 nm chromium, 10 nm gold), and an insulating aluminum oxide layer (ALD, 10 nm). Self-rolling into microtubes was achieved by immersion into a hydrogen peroxide solution for 40 min (concentration ca. 1 % v/v in deionized water), resulting in sensors with a diameter of ca. 30 µm and an array of electrodes encompassing the tube center. Samples were dried with critical point drying to avoid microtube collapse and coated with a final silicon dioxide insulating layer (50 nm) to cover the electrode paths. To connect the sensors to the EIT device, samples were wire-bonded to a custom-made slip-chip adapter. A PDMS frame was bonded around the sensing area to avoid contact between the measurement solution and the bonding wires. Samples to be measured were introduced mechanically into the tube center by using a micromanipulator (PatchMan NP2, Eppendorf) with a glass capillary tip (ICSI Pipettes-Blunt). Phosphate buffered saline (PBS, Sigma–Aldrich) was used as medium.

Principle of Operation – EIT Measurements and Image Reconstruction: In the employed EIT setup, the measurement volume was surrounded by a circularly arranged array of electrodes. Small alternating currents were applied to a selected electrode pair, and the resulting surface voltages were measured at the remaining electrodes. The excitation pair was then subsequently switched until all possible injection patterns were carried out, resulting in individual measurements (the measured potential at the injecting electrodes was disregarded for the image reconstruction to avoid interference with the injection signal). These measurements correspond to one frame, e.g. one cross-sectional image. Using these measurements, the transfer impedances were determined, and a cross-sectional image could be generated. Here, EIT images were generated using a previously described algorithm based on fidelity-embedded regularization (FER).[43] Time-difference EIT was employed, where the conductivity change of the object was measured over time. Specifically, frequency-difference imaging was chosen, where the conductivity change at a specific frequency was monitored, using another frequency as a reference. This was done to avoid

artefacts caused by slight geometry changes in the tube, which might occur during sample insertion with the manipulator or liquid flow.

Measurements were carried out using a fast-sampling EIT device (Sciospec Scientific Instruments GmbH). An electrode pair was excited using an injection current of 1 µA with 20 different frequencies in a range between 100 Hz and 1 MHz, and the resulting potential was measured at the remaining electrodes. A low frame rate of 0.2 frames/second was chosen to ensure the measurement of at least 10 periods per frequency in a given sweep.

Cell Culture: Human epithelial cervical cancer cells (HeLa) were used as model cells to study visualization of cell necrosis. Briefly, HeLa cells were cultured in a suspension flask with medium (DMEM high glucose + 10%FCS + 1% L-Glutamin + 1% PensStrep). For EIT measurements, HeLa suspension cells obtained after splitting were used. Fluorescence microscopy was used as a control to determine cell death. For measurements on necrotic cells, HeLa cells were stained with SYBR 14 dye and propidium iodide (LIVE/DEAD Sperm Viability Kit, ThermoFisher Scientific).

Supporting Information

Supporting Information is available from the Wiley Online Library or from the author.

Acknowledgements

S.M.W. and P.J. contributed equally to this work. The authors would like to thank F. Hebenstreit for support in cell culture and handling, as well as R. Engelhard, B. Eichler, S. Nestler and M. Bauer for clean room and technical support. O.G.S. acknowledges financial support by the Leibniz Program of the German Research Foundation (SCHM 1298/26-1). This work was part of the projects that have received funding from the European Research Council (ERC) under the European Union's Horizon 2020 research and innovation program (grant agreement No. 835268 and 853609).

Open access funding enabled and organized by Projekt DEAL.

Conflict of Interest

The authors declare no conflict of interest.

Data Availability Statement

The data that support the findings of this study are available on request from the corresponding author. The data are not publicly available due to privacy or ethical restrictions.

Keywords

biosensors, electrical impedance tomography, rolled-up microtubes, single-cell analysis

Received: May 9, 2023
Revised: September 16, 2023
Published online: October 18, 2023

[1] S. M. Weiz, M. Medina-Sánchez, O. G. Schmidt, *Microsystems for Single-Cell Analysis*, Vol. *2*, Wiley-VCH Verlag, Weinheim **2018**.
[2] J. Levsky, *Trends Cell Biol.* **2003**, *13*, 4.
[3] S. J. Altschuler, L. F. Wu, *Cell* **2010**, *141*, 559.
[4] S. F. Roerink, N. Sasaki, H. Lee-Six, M. D. Young, L. B. Alexandrov, S. Behjati, T. J. Mitchell, S. Grossmann, H. Lightfoot, D. A. Egan, A. Pronk, N. Smakman, J. Van Gorp, E. Anderson, S. J. Gamble, C. Alder, M. Van De Wetering, P. J. Campbell, M. R. Stratton, H. Clevers, *Nature* **2018**, *556*, 457.
[5] J. R. Heath, A. Ribas, P. S. Mischel, *Nat. Rev. Drug Discovery* **2016**, *15*, 204.
[6] L. C. Kelley, Z. Wang, E. J. Hagedorn, L. Wang, W. Shen, S. Lei, S. A. Johnson, D. R. Sherwood, *Nat. Protoc.* **2017**, *12*, 2081.
[7] K. Giewekemeyer, C. Hackenberg, A. Aquila, R. N. Wilke, M. R. Groves, R. Jordanova, V. S. Lamzin, G. Borchers, K. Saksl, A. V. Zozulya, M. Sprung, A. P. Mancuso, *Biophys. J.* **2015**, *109*, 1986.
[8] R. N. Irobalieva, B. Martins, O. Medalia, *J. Cell Sci.* **2016**, *129*, 469.
[9] A. Kalmykov, C. Huang, J. Bliley, D. Shiwarski, J. Tashman, A. Abdullah, S. K. Rastogi, S. Shukla, E. Mataev, A. W. Feinberg, K. J. Hsia, T. Cohen-Karni, *Sci. Adv.* **2019**, *5*, eaax0729.
[10] C. C. Barber, B. H. Brown, I. L. Freeston, *Electron. Lett.* **1983**, *19*, 933.
[11] B. Brown, *J. Med. Eng. Technol.* **2003**, *27*, 97.
[12] S. Hannan, M. Faulkner, K. Aristovich, J. Avery, M. C. Walker, D. S. Holder, *NeuroImage* **2020**, *209*, 116525.
[13] S. Hannan, M. Faulkner, K. Aristovich, J. Avery, M. Walker, D. Holder, *NeuroImage: Clin.* **2018**, *20*, 674.
[14] S. Hannan, K. Aristovich, M. Faulkner, J. Avery, M. C. Walker, D. S. Holder, *Physiol. Meas.* **2021**, *42*, 014001.
[15] M. Faulkner, S. Hannan, K. Aristovich, J. Avery, D. Holder, *NeuroImage* **2018**, *178*, 1.
[16] M. Faulkner, S. Hannan, K. Aristovich, J. Avery, D. Holder, *Physiol. Meas.* **2018**, *39*, 034007.
[17] K. Y. Aristovich, B. C. Packham, H. Koo, G. S. D. Santos, A. Mcevoy, D. S. Holder, *NeuroImage* **2016**, *124*, 204.
[18] T. A. York, T. N. Phua, L. Reichelt, A. Pawlowski, R. Kneer, *Meas. Sci. Technol.* **2006**, *17*, 2119.
[19] Y. Granot, A. Ivorra, E. Maor, B. Rubinsky, *Phys. Med. Biol.* **2009**, *54*, 4927.
[20] T. Sun, S. Tsuda, K.-P. Zauner, H. Morgan, *Biosens. Bioelectron.* **2010**, *25*, 1109.
[21] E. J. Smith, W. Xi, D. Makarov, I. Mönch, S. Harazim, V. A. Bolaños Quiñones, C. K. Schmidt, Y. Mei, S. Sanchez, O. G. Schmidt, *Lab Chip* **2012**, *12*, 1917.
[22] E. J. Smith, S. Schulze, S. Kiravittaya, Y. Mei, S. Sanchez, O. G. Schmidt, *Nano Lett.* **2011**, *11*, 4037.
[23] A. I. Egunov, Z. Dou, D. D. Karnaushenko, F. Hebenstreit, N. Kretschmann, K. Akgün, T. Ziemssen, D. Karnaushenko, M. Medina-Sánchez, O. G. Schmidt, *Small* **2021**, *17*, 20012549.
[24] E. Ghosh, A. I. Egunov, D. Karnaushenko, M. Medina-Sánchez, O. G. Schmidt, *Frequenz* **2022**, *76*, 729.
[25] C. S. Bausch, C. Heyn, W. Hansen, I. M. A. Wolf, B.-P. Diercks, A. H. Guse, R. H. Blick, *Sci. Rep.* **2017**, *7*, 41584.
[26] C. S. Martinez-Cisneros, S. Sanchez, W. Xi, O. G. Schmidt, *Nano Lett.* **2014**, *14*, 2219.
[27] M. Medina-Sánchez, B. Ibarlucea, N. Pérez, D. D. Karnaushenko, S. M. Weiz, L. Baraban, G. Cuniberti, O. G. Schmidt, *Nano Lett.* **2016**, *16*, 4288.
[28] B. Koch, A. K. Meyer, L. Helbig, S. M. Harazim, A. Storch, S. Sanchez, O. G. Schmidt, *Nano Lett.* **2015**, *15*, 5530.
[29] Z. Chen, G. Huang, I. Trase, X. Han, Y. Mei, *Phys. Rev. Appl.* **2016**, *5*, 017001.
[30] G. Huang, Y. Mei, *Small* **2018**, *14*, 1703665.
[31] Ch. Deneke, C. Müller, N. Y. Jin-Phillip, O. G. Schmidt, *Semicond. Sci. Technol.* **2002**, *17*, 1278.
[32] S. M. Weiz, M. Medina-Sánchez, O. G. Schmidt, *Adv. Biosyst.* **2018**, *2*, 1700193.

[33] M. Takahashi, C. Figus, L. Malfatti, Y. Tokuda, K. Yamamoto, T. Yoko, T. Kitanaga, Y. Tokudome, P. Innocenzi, *NPG Asia Mater* **2012**, *4*, e22.
[34] C. N. Saggau, F. Gabler, D. D. Karnaushenko, D. Karnaushenko, L. Ma, O. G. Schmidt, *Adv. Mater.* **2020**, *32*, 2003252.
[35] G. L. Long, J. D. Winefordner, *Analy. Chem.* **1983**, *55*, 712A.
[36] M. A. Denaï, M. Mahfouf, S. Mohamad-Samuri, G. Panoutsos, B. H. Brown, G. H. Mills, *IEEE Trans. Inf. Technol. Biomed.* **2010**, *14*, 641.
[37] R. H. Bayford, *Annu. Rev. Biomed. Eng.* **2006**, *8*, 63.
[38] A. Adler, A. Boyle, *IEEE Trans. Biomed. Eng.* **2017**, *64*, 2494.
[39] R. Bounik, F. Cardes, H. Ulusan, M. M. Modena, A. Hierlemann, *BME Front* **2022**, *2022*, 9857485.
[40] M. Schwarz, M. Jendrusch, I. Constantinou, *Electrophoresis* **2020**, *41*, 65.
[41] X. Yin, H. Wu, J. Jia, Y. Yang, *IEEE Sens. J.* **2018**, *18*, 5402.
[42] T. Oh, O. Gilad, A. Ghosh, M. Schuettler, D. S. Holder, *Med. Biol. Eng. Comput.* **2011**, *49*, 593.
[43] K. Lee, E. J. Woo, J. K. Seo, *IEEE Trans. Med. Imaging* **2017**, *37*, 1970.
[44] G. Kroemer, L. Galluzzi, P. Vandenabeele, J. Abrams, E. S. Alnemri, E. H. Baehrecke, M. V. Blagosklonny, W. S. El-Deiry, P. Golstein, D. R. Green, M. Hengartner, R. A. Knight, S. Kumar, S. A. Lipton, W. Malorni, G. Nuñez, M. E. Peter, J. Tschopp, J. Yuan, M. Piacentini, B. Zhivotovsky, G. Melino, *Cell Death Differ.* **2009**, *16*, 3.

Single-Cell Impedence Tomography Using Rolled-Up Microtubolar Sensors

In a nutshell:

Objective: to characterize the electrical properties of individual cells to study cellular heterogeneity that occurs between cells of the same tissue

Requirements: Single-cell analysis should be non-destructive and label-free to allow long-term measurements that do not alter the cell functions

Achievements: fabrication of a micro electrical impedance tomography (EIT) system via rolled-up nanotechnology + proof-of-concept measurements with silica or Janus particles and cancer cells

Sum up of the system: 30μm diameter ( ) tube containing an array of 12 electrodes on its interior wall, where can be tuned during the fabrication process

Outlooks: using the system to study the efficiency of drugs or the biocompatibility of materials on a single-cell level

Introduction

In biology, animal or human cells are found at the microscale, in the order of 10-20μm. Typical analysis through standard large cell cultures methods allows for quite high output signals due to the presence of a large number of cells. While high signal-to-noise ratio (SNR), provided by cell culture methods is a desirable feature for cell analysis, this method neglects cellular heterogeneity within a population. However, this assumption neglects possible differences within the cell culture population, also identified as cellular heterogeneity. In this context, large scale measurements become a downside because they can hide important cells' features essential for the organism's characterization.

For this reason, innovative techniques for realizing single-cell analysis have been pursued in recent years worldwide. In theory, single-cell analysis devices provide high sensitivity and resolution useful to detect -among all- abnormalities of individual cells, for example. In this scenario, one could prevent difficult-to-treat illnesses, such as cancer, from further developing thanks to early detection.

Among the wide range of analysis methods, tomographic measurements provide spatially resolved localized information, like whole-cell or cell-parts movements. Combining multi-electrode impedance and topographic measurements, one can obtain the best tool for studying communication among single cells or cell parts. Conductivity distribution of an object is imaged thanks to this kind of method, also called Electrical Impedance Tomography (EIT). In this

case, it is the conductivity to be measured, differently from electrophysiological methods where an ionic current is detected across the cell membrane. Advantages over the aforementioned technique are that EIT is label-free, non-destructive, and provides real-time information and long-term monitoring. The only disadvantage is the lower image resolution. In real life, EIT technique has found great use in medical setups such as pulmonary, gastric and neurological imaging. However, none of such devices has been able to detect a single animal or human cell, notably in the order of 10μm range. To this aim, the following research brings novelty in the field of EIT sensors in the sub-100μm size range by exploiting self-assembled roll-up of strained nanometer thin films.

Basics of the fabrication process of such a device include photolithography and thin film deposition to pattern an EIT electrode array into a small 3D structure. Then, to perform imaging an AC current is applied to a pair of electrodes. To reconstruct a map of conductivity distribution, voltages across sequential electrode-pair combinations are collected. Placement of interdigitated electrodes inside the tubular structure increases the sensitivity and SNR, while decreasing the limit of detection (LoD) in comparison to the conventional coplanar electrode topologies,

Fabrication parameters, such as tubular geometry or use of transparent materials, can increase sensitivity and mimic in vivo constraints, enabling measurements under physiological conditions. Validity of this approach is demonstrated by using either silica or Janus particles and cancer cells. Versatility of the technique to measure conductivity changes is demonstrated by testing living biological samples over time, like cell necrosis.

Future works include the analysis of drugs effects on the cell behaviour in live and real-time imaging. This method allows for label-free imaging of particles at single-cell/particle level with high accuracy.

Results and Discussion

I. μEIT fabrication

Fabrication techniques involved in the article: Photolithography, PVD, ALD, WE, critical-point drying

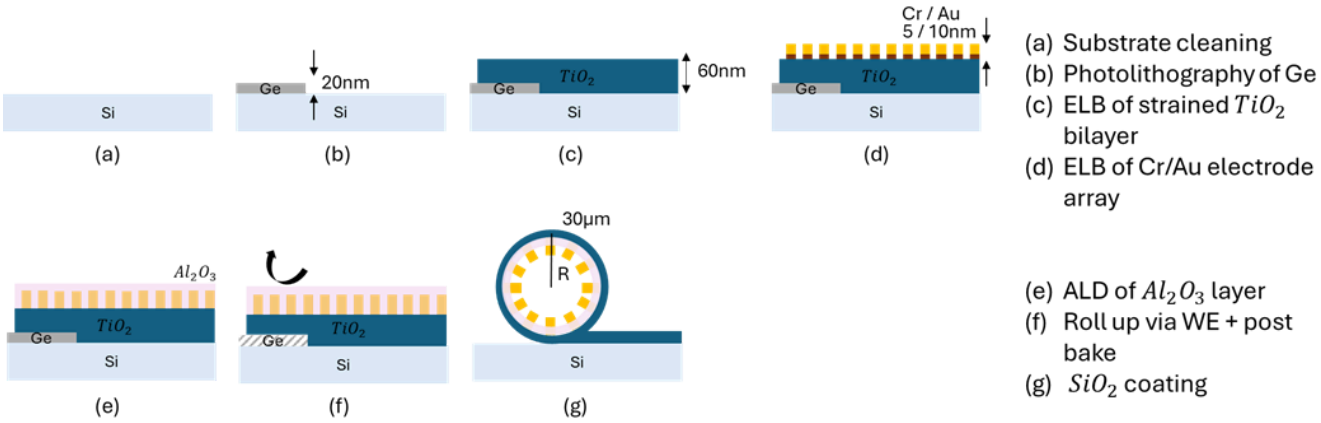

Figure 1. Process flow

Ge(20nm), TiO2(60nm), Cr(5nm), Au(10nm) and SiO2(50nm) are all deposited via e-beam PVD. e-beam is one way to heat up the material to evaporate in thermal evaporation. In the e-beam method, an anode accelerates electrons which are driven towards the crucible in a controlled manner via magnetic fields. The material to deposit is heated by the electrons and evaporates from the crucible. Eventually, it condenses on the substrate to form a thin film. By using e-beam heating, higher purity films can be created.

N°	Category	Recipe	T° [°C]	base press [mbar]	O_2 [sccm]	Dep. IAD	Material	Crucible	dep. rate Å/s	Max (kÅ)
350	HRN	TiO2	RT	2.00E-06	10		Ti3O5	4	3.0	5.000
241	HRN	Ge	RT	2.00E-06			Ge	4	4.0	5.000
130	HRN	Cr	RT	1.50E-06			Cr	2	4.0	2.000
181	HRN	Au	RT	2.00E-06			Au	3	4.0	5.000
250	HRN	SiO2	RT	2.00E-06			SiO2	1	4.0	5.000

Figure 2. Process parameters used in CMi for the same materials mentioned in the paper (thermal evaporation data)

Al2O3 as insulating material to define the working window. AlO3 is an excellent insulator, with a high dielectric strength. This property significantly reduces leakage currents, which enhances the accuracy of impedance measurements by minimizing unwanted electrical pathways. As a consequence, higher signal to noise ratios are achieved.
Al2O3 is deposited via ALD. Atomic Layer Deposition includes two reaction steps in sequence. Both steps are self-limiting processes. One cycle (=2 reaction steps) creates about 1nm thick layer. So, to obtain a 10nm thick layer ALD is performed around 10 times. In the case of Al2O3, the gas used are Trimethyl Aluminum Al(CH3)3 and H2O vapor.

H2O2 wet etching to achieve self-rolling of the structure. The solution contains 1% v/v H2O2 in DIW. Samples are kept there for 40min. Ge is etched slowly by water, which leads to more compact and stable tubular structures during the rolling process.
Drying of etching is carried out by means of **supercritical point drying method** to avoid unwanted permanent deformation (collapsing) of the surface-micromachined structure. Critical point drying includes the following steps:

1. Replace H2O2 solution with ethanol (RT)
2. Place the sample in a closed chamber that is filled with CO2 gas
3. Decrease T_chamber at 10°C
4. Increase P to 75bar (A→B)
5. Increase T to 31 ºC, that is the critical point temperature of CO2 (B→C). P rises to 93 bar and a supercritical fluid is formed. There is no distinction between liquid and gas phase → hence no surface tension!
6. Decrease P during a 4 min process (C→D), in which the CO2 evaporates
7. Decrease T to to RT (D→E)

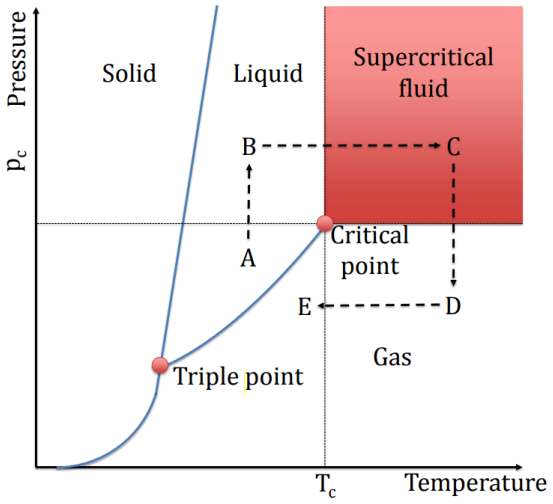

Figure 3. Critical point drying method

Possible photolithography process flow in CMI includes the following parameters:

- Spin coat parameters:

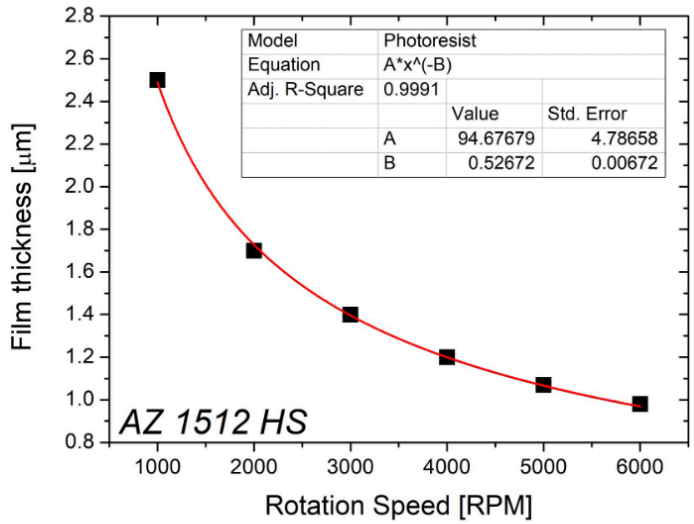

AZ1512HS photoresist - recommended for wet etching → good adhesion profile

- Exposure parameters:

Illumination:	**Broadband***	**i-line (355-365 nm)**	**h-line (405 nm)**
Equipment:	**MABA6, MA6 Gen3 (no filter)**	**VPG 200, MA6 Gen3 (filter), MJB4**	**MLA 150**
PR thickness [µm]	**Dose [mJ/cm^2]$^+$**	**Dose [mJ/cm^2]$^{++}$**	**Dose [mJ/cm^2]$^{+++}$**
1.1	30	32	Refer to Resist Tables
1.3	40	42	
1.5	47	49	
1.6	50	52	
2	60	64	
2.6	80	85	

** Mercury Lamp, Mask Aligner with UV400 configuration & no filter / + Based on intensity readings from Süss optometer broadband CCD / ++ Based on intensity readings from Süss optometer i-line CCD / +++ Based on MLA150 internal dose measurements*

- Development parameters:

Automatic development on EVG 150

Development recipes for AZ 1512 HS (identical for all are **AZ1512_1to2um_*** databases) are listed below:

Recipe name	PR thickness [µm]	Total contact time [s]
D4_HB_1512_1u1_PUD	1.1	40
D4_HB_1512_1u3_PUD	1.3	45
D4_HB_1512_1u5_PUD	1.5	50
D4_HB_1512_1u6_PUD	1.6	55
D4_HB_1512_2u_PUD	2	65
D4_HB_1512_2u6_PUD	2.6	75

The developement consists of a short spray dispense followed by puddle method. To maintain a high wafer throughput on the EVG 150, no hardbake is applied for standard AZ1512 recipes.

AZ 726 MIF is recommended as a developer for the aforementioned photoresist. No hardbake afterwards for wet etching. Critical drying method is used instead.

II.µEIT Electrode Characterization:

In relation to the course content, although not completely mentioned, following characterization techniques were / might have been realized in realization of the structure.

- Optical microscopy: Brightfield microscopy should have been used after each fabrication step to check for possible errors. In addition, cell experiments were monitored by fluorescent microscopy for viability analysis.
- SEM: After tubular structure was formed, the 3D structure was imaged using SEM to measure the size and analyze its integrity.
- Mechanical characterization: Since formation of the tubular structure depends on stress gradient between 2 layers, at least to optimize the fabrication parameters, the stress on each layer should have been measured with laser beam surface profiler. (This is not mentioned in the paper but for the aforementioned tubular structure this analysis is necessary)
- Electrochemical characterization: Cyclic voltammetry tests were done to measure electrochemical performance of the structure, using Janus particles- current-voltage plots are generated.

III.EIT Tomography and Detection Modes: definition of EIT

EIT means electrical Impedance Tomography and it is a non-invasive technique that allows the imaging of conductivity, permittivity and impedance maps of the sample. All those properties depend on the sample free ion content.

The proposed device permits the monitoring of small objects or single cells (size range 30um). It involved the application of small AC currents at different frequencies through electrodes 1 and 2. The resulting equi-potentials are recorded from the remaining pairs of electrodes (1-4 and 7-12).

3 reported modes are used:

1. absolute or static EIT (a-EIT) to measure the absolute conductivity distribution of the analysed sample. Limitation: partial losses of I leading to noise/artifacts.
2. Differential EIT to record data of the same sample between 2 or more different states.

2.a. Time-differential EIT measures conductivity as a function of time → use for cancer cell death monitoring over time

2.b. Frequency-difference EIT (fd-EIT) measures conductivity as a function of frequency → use for phantom sample characterization

IV. Detection of Cell Death Using the μEIT

Cell viability is ensured by fluorescence imaging-cell is stained before introduction into the structure so that it is known that the cell is alive or not during the experiments - optical verification. Cell is placed inside PBS with no nutrients - cell membrane becomes permeable and PBS enters the cytoplasm of the cell, changing the conductivity distribution-hence cell death is measured based on the conductivity.